OPEN ACCESS

ACTA METALLURGICA SLOVACA

2026, VOL. 32, NO. 1, 33-40

RESEARCH PAPER

Feasibility of inconel and carbon steel dissimilar welded joint

Sakuntala Nahak[1], Anmol Bhatia[2], Saurabh Dewangan[3]*

[1, 2]Department of Multidisciplinary Engineering, The Northcap University, Gurugram, Haryana, India, Pin-122017

[*3]Department of Mechanical Engineering, Manipal University Jaipur, Jaipur, Rajasthan, India, Pin-303007

*Corresponding author: saurabh.dewangan@jaipur.manipal.edu, tel.: 0141-3999100-838, Department of Mechanical Engineering, Manipal University Jaipur, Jaipur, Rajasthan, India, Pin-303007

Received: 25.11.2025
Accepted: 27.02.2026

ABSTRACT

This study investigates the weldability, microstructural evolution, and tensile performance of six different welded joint configurations involving Inconel 718 (IN) and AISI 1018 carbon steel (CS). The tensile results show significant variation across the joints. Optical microscopy revealed dendritic weld structures in IN-rich zones, ferrite–pearlite transformations in CS HAZ, and heterogeneous solidification patterns where filler–substrate mismatch was high. The originality of this work lies in its direct comparison of similar and dissimilar IN–CS joints using two filler metals, correlating mechanical performance with dilution effects, dendritic morphology, and trends in carbide/Laves phase formation.

Keywords: Dissimilar Metal Welding; Inconel; Carbon Steel; Microstructural Analysis; Mechanical Properties

1. Introduction

The joining of dissimilar metals is becoming increasingly important in engineering applications, especially in the aerospace and automotive sectors. Among the different metal pairings, welding Inconel with plain carbon steel presents both challenges and opportunities. Inconel 718 is preferred in high-performance environments because it can maintain its strength even at very high temperatures (**Fig. 1**), whereas carbon steel remains a widely used material due to its low cost and dependable structural performance in general engineering applications (**Fig. 2**).

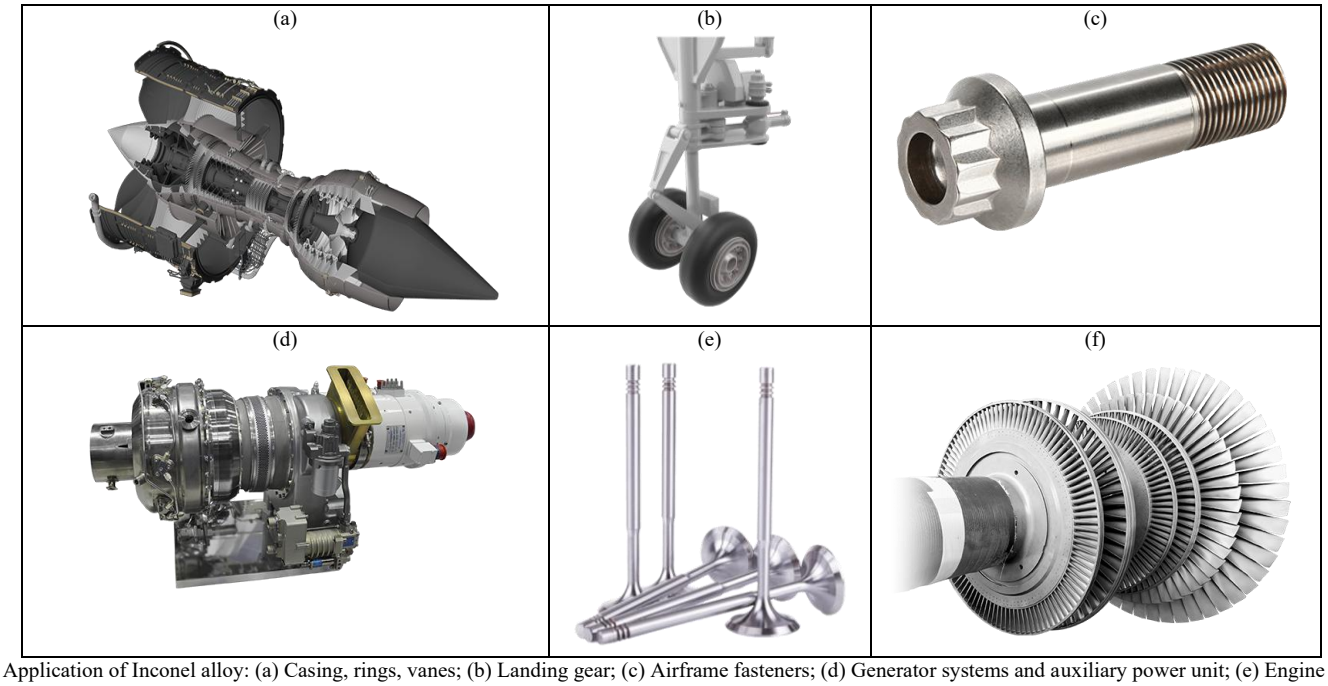

Fig. 1 Application of Inconel alloy: (a) Casing, rings, vanes; (b) Landing gear; (c) Airframe fasteners; (d) Generator systems and auxiliary power unit; (e) Engine Valves; (f) Turbine blades and discs [1]

Fig. 2 Industrial applications of carbon steel [2, 3]

The dissimilar joint between Inconel and plain carbon steel has been very little explored due to metallurgical challenges that occurred during the welding process, although the welded joint between Inconel and stainless steel has now become widely adopted. The metallurgical compatibility between Inconel and stainless steel is considered favorable due to their shared austenitic structure, which includes an FCC crystal structure and similar thermal expansion characteristics [4, 5]. This compatibility facilitates effective welding, typically using filler metal made up of Inconel alloy itself, which helps preserve both corrosion resistance and mechanical strength. Additionally, the dilution zone at the weld interface remains chemically stable, reducing the likelihood of brittle phase formation or cracking and thereby ensuring structural integrity. The Inconel-stainless steel joints are suitable for aerospace, chemical, and nuclear industries [6, 7].

In contrast, Welding Inconel to carbon steel presents significant metallurgical challenges due to stark differences in their microstructural and thermal properties. Carbon steel, typically ferritic or pearlitic with a BCC structure and high carbon content [8, 9], contrasts sharply with Inconel's face-centered cubic (FCC) structure [10]. During welding, carbon tends to migrate from the steel into the Inconel, forming hard and brittle carbides such as NbC, MoC, and $Cr_{32}C_6$ at the fusion boundary. These carbides contribute to cracking in the heat-affected zone (HAZ), loss of ductility, and reduced corrosion resistance. Additionally, the mismatch in thermal expansion coefficients between the two materials induces residual stresses, further compromising weld integrity [11, 12]. Microstructural studies reinforce these concerns: Bagchi et al. (2025) reported 30% iron dilution and NbC intermetallic formation in Inconel 625 overlays on AISI 4140 steel, highlighting risks of cracking and corrosion [13]. Sedighi et al. (2019) observed bainite formation in the HAZ of carbon steel welded to Inconel 625, which transformed into ferrite-pearlite after stress relief, yet complex carbides persisted, degrading weld quality [14]. Rathod et al. (2016) emphasized the necessity of buffer layers such as Ni–Fe to mitigate carbon diffusion and metallurgical deterioration in ferritic–Inconel welds [15]. These incompatibilities often render the joint less reliable and necessitate advanced welding techniques or buffer layers.

In view of the incompatibilities of arc welding, various bonding and overlay techniques, including roll bonding, explosive cladding, friction welding, weld overlay, and friction stir lap welding, have been widely investigated, with heat treatment methods, to improve joint integrity. Studies have shown that welding parameters and post-weld heat treatment (PWHT) strongly affect the resultant microstructure and properties. For example, Guo et al. (2021) found that PWHT at 650°C provided optimal corrosion resistance and ductility for Inconel 625/AISI 4130 bimetal plates, whereas higher PWHT temperatures increased the corrosion rate and coarsened the microstructure [16]. Investigations on FCAW-based overlay welding demonstrated that heat input strongly influences weld deformation, dilution, and required finishing operations [17]. Research on friction stir lap welding between GL E36 steel and Inconel 625 revealed that Fe–Ni mechanical mixing acts as the primary bonding mechanism and that thermal cycles govern microhardness, lap-shear behavior, and residual stresses [18]. Stress-relief studies on Inconel 625–A106 joints further demonstrated transformations from bainite to ferrite–pearlite and increased carbide precipitation at higher temperatures [19]. Additional work on PWHT of Inconel 182 overlays on AISI 4130 indicated enhanced elemental diffusion and reduced hardness mismatch after treatment at 640°C for three hours [20]. Investigations on SAW and GMAW overlays consistently emphasized that lower heat inputs reduce cracking, control dilution, and improve hardness distribution [21–22]. Explosive-welded joints treated through annealing or normalizing exhibited distinct recrystallization patterns and diffusion zone morphologies, while TIG-welded AISI 1020–Inconel 718 joints showed columnar ferrite in the weld zone and intermediate mechanical properties between the similar-metal joints [23–24]. Supporting literature also highlights that optimized heat input, travel speed, shielding environment, and filler selection (e.g., ERNiCrMo-3, ERNiFeCr-2), along with interlayers, mitigate metallurgical incompatibilities during Inconel–steel welding [25–27].

The feasibility of forming sound welded joints between Inconel 718 and carbon steel is primarily governed by metallurgical compatibility, which is inherently limited due to their differing alloy chemistries and crystal structures. Inconel 718 possesses an FCC structure strengthened by γ″ and γ′ phases, whereas carbon steel exhibits a BCC lattice with higher carbon diffusivity. During welding, carbon from steel migrates into the Inconel-rich fusion boundary, promoting the formation of hard carbides such as NbC, MoC, and $Cr_{32}C_6$, while iron dilution encourages formation of Laves and Fe–Ni intermetallic compounds—both detrimental to toughness and ductility [28, 29]. Thermal expansion mismatch further produces residual stresses that weaken joint integrity. Microstructurally, the fusion zone typically solidifies with dendritic growth and segregation of niobium and molybdenum, favouring brittle Laves-phase formation [30]. The Inconel HAZ may exhibit δ-phase precipitation and grain boundary instability, whereas the carbon steel HAZ can undergo martensitic transformation or grain refinement, resulting in sharp hardness gradients and crack initiation sites. The interfacial region is especially vulnerable to unmixed zones and abrupt compositional transitions, making controlled heat input and buffer layers essential [23]. A study reported distinctive microstructural features in TIG-welded Inconel–carbon steel joints, including refined ferrite–pearlite in the carbon steel HAZ, γ and δ phases with prominent austenite twins in the Inconel base metal, and a serrated ferrite morphology in the weld zone with increased ferrite content and absence of pearlite [24].

Existing literature highlights significant metallurgical incompatibilities between Inconel alloys and carbon steels, including carbon migration, carbide formation, elemental segregation, and residual stress development, all of which negatively influence weld integrity. Previous studies also emphasized the need for optimized heat input, buffer layers, and controlled dilution to minimize brittle phases such as carbides and Laves compounds during dissimilar welding.

The objective of this study is to systematically evaluate the weldability, microstructural evolution, and mechanical performance of similar (IN–IN, CS–CS) and dissimilar (IN–CS) TIG-welded joints produced using two different filler metals—Inconel 718 and low-carbon steel—and to determine how dilution, solidification behavior, and phase formation influence joint integrity. The originality of this work lies in its comprehensive, side-by-side comparison of six distinct welded configurations, enabling a unique correlation between tensile properties, weld-zone microstructures, HAZ transformations, and the likelihood of brittle phases such as carbides and Nb-rich Laves compounds.

2. MATERIALS AND METHODOLOGY

The present work involves six plates of Inconel 718 alloy (IN) and six plates of AISI 1018 carbon steel (CS), each with identical dimensions of 50 × 50 × 3 mm. A total of six pairs of plates were joined using TIG welding. The welding parameters selected were a current of 140 A and a voltage of 14 V. Argon gas with 99% purity was used as shielding gas. For each pair, the adjoining butt surfaces were machined to a 50° groove angle. Two types of filler wires were employed in this study: a 2 mm Inconel 718 alloy wire and a 2 mm copper-coated Mn–Si alloyed low-carbon steel wire. The choice of filler wire varies for each welded pair. The sample naming for similar and dissimilar welded joints with two different filler metals is shown in **Table 1**.

Standard tensile specimens were extracted from each welded plate using a wire-cut machining process. All specimens were prepared in accordance with the ASTM E8 guidelines. Tensile testing was carried out on an FIE Universal Testing Machine (Model: UTES 40 HGFL, Serial No. 7/2019-6284), which has a maximum load capacity of 40 kN. Photographs of the specimens before and after testing are presented in Fig. 3. The load–displacement curves for all samples were generated using the data acquisition system integrated with the testing machine.

Table 1 Sample naming for different welded plates

Sr. No.	Sample	Welding condition	Graphical representation
1	*Sample 1 (S1)*	Welded joint between Inconel 718 and Inconel 718 with filler wire of Inconel 718	IN / IN IN
2	*Sample 2 (S2)*	Welded joint between Inconel 718 and Inconel 718 with filler wire of low carbon steel	CS / IN IN
3	*Sample 3 (S3)*	Welded joint between Inconel 718 and low carbon steel with filler wire of Inconel 718	IN / IN CS
4	*Sample 4 (S4)*	Welded joint between Inconel 718 and low carbon steel with filler wire of carbon steel	CS / IN CS
5	*Sample 5 (S5)*	Welded joint between low carbon steel and low carbon steel with filler wire of Inconel 718	IN / CS CS
6	*Sample 6 (S6)*	Welded joint between low carbon steel and low carbon steel with filler wire of low carbon steel	CS / CS CS

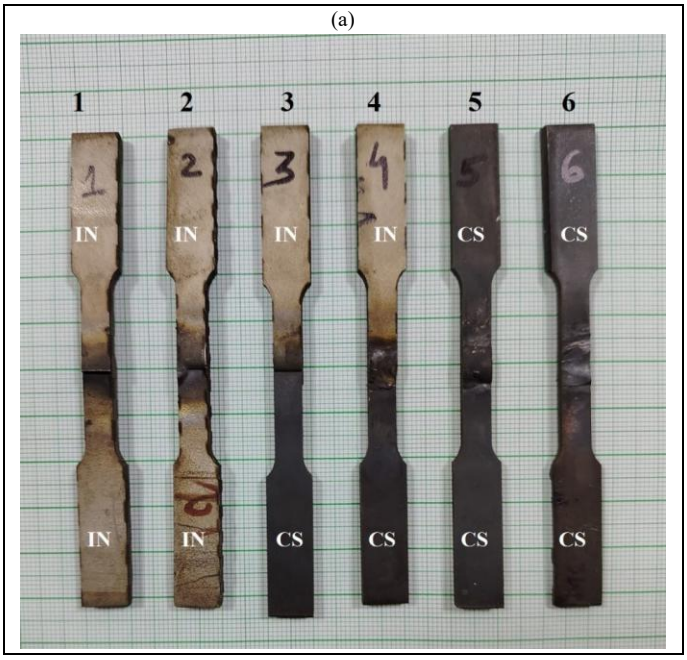

Fig. 3: Tensile test specimens: (a) Before the test; (b) After the test

A small section was removed from each welded plate in such a way that all three characteristic regions—base metal, weld metal, and heat-affected zone (HAZ)—were included. The cross-sectional surface of each sample was subsequently polished using standard metallographic procedures to obtain a mirror-like finish suitable for microscopic examination. As the welded joints consisted of two different alloys, distinct etchants were used to reveal the microstructure. Nital (2% nitric acid in ethanol) was used for etching the carbon steel region, while the Inconel area was etched using a solution comprising nitric acid (50 mL), hydrochloric acid (70 mL), 30% hydrogen peroxide (35 mL), and distilled water (90 mL). Etching was performed for approximately 5–10 seconds using a cotton swab to ensure uniform attack across the surface.

3. RESULT ANALYSIS

Tensile test result: Six welded joint configurations involving Inconel 718 and low-carbon steel (CS) were tensile-tested. Tensile metrics (UTS, YS, %El) and the load-displacement curves were obtained directly from the machine for Samples 1–6. Importantly, Samples 1–5 fractured through the welded joint, whereas Sample 6 failed from the base metal (BM) side, indicating that the weld in Sample 6 exceeded the strength of the parent material. The tensile properties of the six welded plates are written in **Table 2**. Also, the load-displacement curves are shown in **Fig. 4**.

Table 2 Tensile metrics obtained from different joints

Sample	Joint	Filler metal	Ultimate tensile strength, UTS (MPa)	Yield stress, YS (MPa)	Elongation (%)
S1	Inconel 718 – Inconel 718	IN	238.664	212.739	1.84
S2	Inconel 718 – Inconel 718	CS	169.995	159.052	1.36
S3	Inconel 718 – CS	IN	287.729	203.960	1.56
S4	Inconel 718 – CS	CS	347.859	275.389	19.25
S5	CS – CS	IN	357.254	288.727	2.76
S6	CS – CS	CS	414.621	301.715	27.08

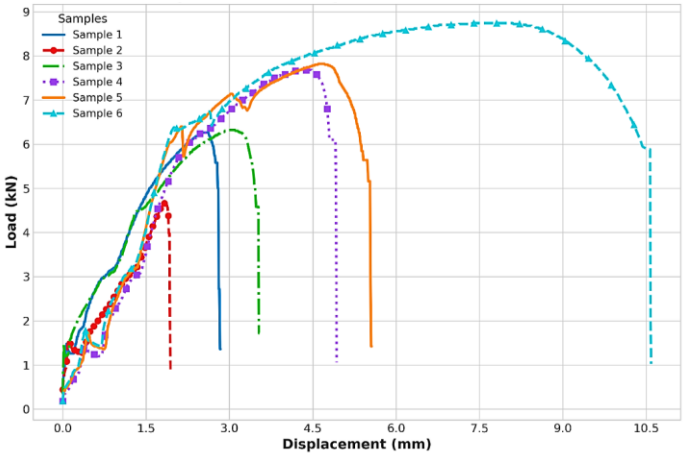

Fig. 4: Outcome of tensile test in the form of load-displacement curves

Analysis between IN – IN Joints (Samples 1 & 2): S1 shows significantly higher UTS (+40.39 %), YS (+33.75 %), and elongation (+35.29 %) over S2. Both samples fractured within the weld metal, confirming that the joint was the weakest region in both cases. However, the inferior performance of S2 indicates that using an LCS filler with Inconel greatly reduces weld integrity. The load-displacement curves further show early load drop in S2 and poor post-yield behavior. Hence, a matching Inconel 718 filler is essential for maintaining weld strength in Inconel–Inconel joints.

Analysis between IN– CS (Dissimilar Joints: Samples 3 & 4): S4 significantly outperforms S3 in tensile strength (+20.9 %), yield strength (+35 %) and especially ductility (+1134%). Despite this large improvement, S4 still fractures at the weld joint, indicating that—even with optimal filler—the dissimilar weld remains the critical failure zone. The superior performance of S4 arises due to better metallurgical compatibility of CS filler on the steel side and reduced mismatch stresses compared to an Inconel-rich weld (S3). Load-displacement curves show S4 with a markedly longer post-yield region and higher peak load than S3. For dissimilar Inconel–LCS joints, carbon-steel filler produces significantly better tensile and ductility performance than Inconel filler, but the weld zone remains the limiting region.

Analysis between CS – CS (Samples 5 & 6): S6 shows the highest UTS (414.6 MPa), highest YS (301.7 MPa), and highest elongation (27.08%) among all samples. Importantly, Sample 6 fractures in the base metal, not the weld, indicating that the welded joint in Sample 6 is stronger than the parent metal. In contrast, S5 (Inconel-filled) fails within the weld, indicating severe metallurgical mismatch and poor weld plasticity. The load–displacement curve of S6 shows the largest displacement and highest peak load of all samples, confirming superior energy absorption and ductile behavior.

Microstructural result: All the optical microscopic images were captured at a common magnification of 100 X and at a common scale that is mentioned on each image. The microstructure of the base metal of Inconel 718 and AISI 1018 steel is shown in **Fig. 5**.

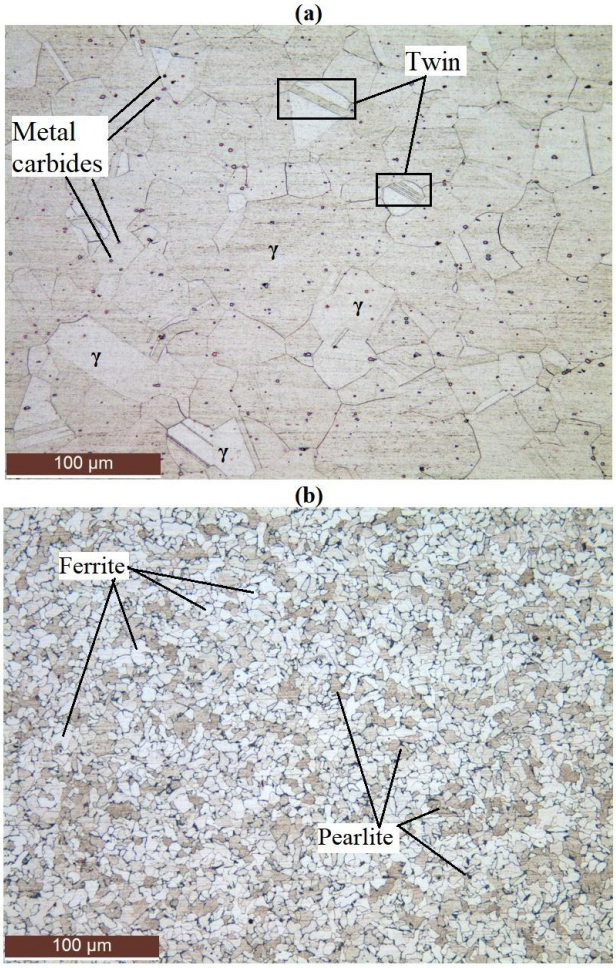

Fig. 5 (a) Microstructure of base metal of Inconel 718 (IN); (b) Microstructure of base metal of AISI 1018 (CS) low carbon steel

The microstructure of Inconel 718 exhibits a typical austenitic matrix (FCC Ni-based solid solution) with a uniform distribution of fine equiaxed grains [31, 32]. The image shows annealing twins, which are characteristic of nickel-based alloys due to their low stacking fault energy. The grains appear clean and free from coarse precipitates, consistent with a wrought condition. However, the presence of black spots is due to metal carbides [33-35]. The uniform grain structure indicates that no local deformation or heat-affected zone changes have occurred yet. The twinning and equiaxed grains together confirm the stable austenitic microstructure of IN (**Fig. 5a**).

The microstructure of the base metal of AISI 1018 low-carbon steel is shown in Fig. 5(b). The carbon steel microstructure clearly shows the expected ferrite–pearlite morphology [36]. Ferrite appears as bright regions, while pearlite colonies—alternating ferrite/cementite lamellae—appear as darker patches. The ferrite content is relatively high, consistent with 0.18% carbon steel. Pearlite colonies are uniformly distributed and do not show deformation or abnormal grain growth, confirming a stable low-carbon steel microstructure [37, 38].

Analysis of an IN–IN welded plate using an IN filler: The HAZ on the Inconel 718 side shows noticeable grain coarsening due to the high heat input. The grains near the fusion boundary are larger and elongated, suggesting partial recrystallization and grain growth. The presence of annealing twins is retained, but they become less dense as grains coarsen. No melted-and-solidified structure is visible, confirming this is HAZ (**Fig. 6a**). The weld zone exhibits a dendritic solidification structure, typical for nickel-based alloy welds. Columnar dendrites appear to grow from the fusion boundary toward the weld center. The dendritic arms are clearly visible, indicating directional heat flow during solidification. The microstructure is homogeneous because the filler and plates are both IN, resulting in metallurgical compatibility and uniform solidification (**Fig. 6b**).

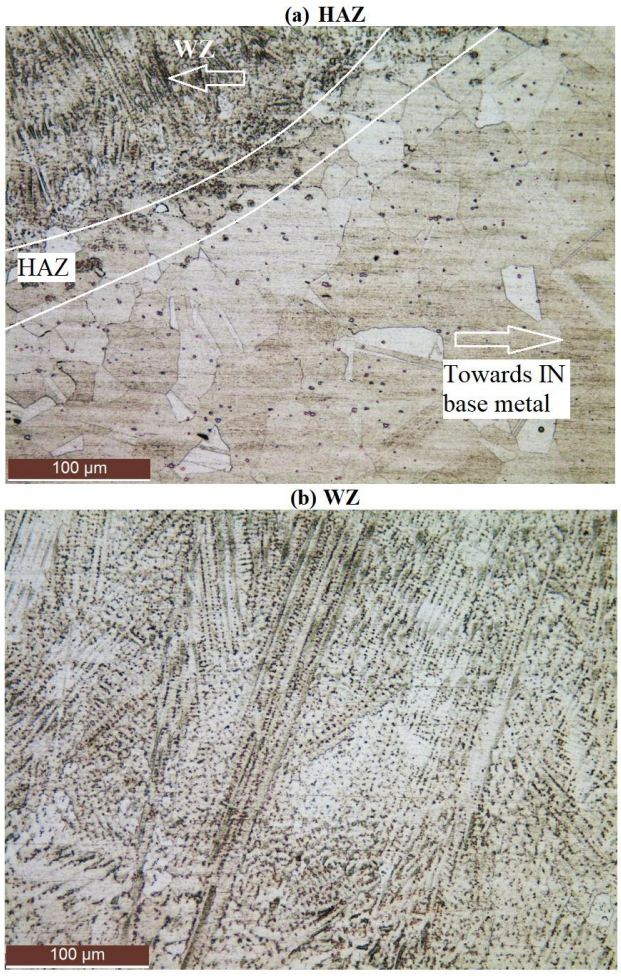

Fig. 6 Microstructural image of IN-IN welded plate with filler metal of IN: (a) Heat-affected zone; (b)Welded zone

Analysis on IN–IN welded plate using CS filler: Like **Fig. 6(a)**, the HAZ shows grain coarsening, but the extent appears slightly more pronounced. This is expected when using a CS filler because the weld metal solidification behavior changes, leading to altered thermal gradients. Twins within large grains are visible but less distinct (**Fig. 7a**). The weld zone has a mixed solidification morphology. Unlike IN filler, the CS filler introduces Fe-rich composition, leading to the formation of dendrites with different contrast, possibly indicating segregation during solidification. The weld pool solidified with a higher tendency for ferrite formation due to the Fe-based filler. This results in a more heterogeneous dendritic structure compared to IN filler (**Fig. 7b**).

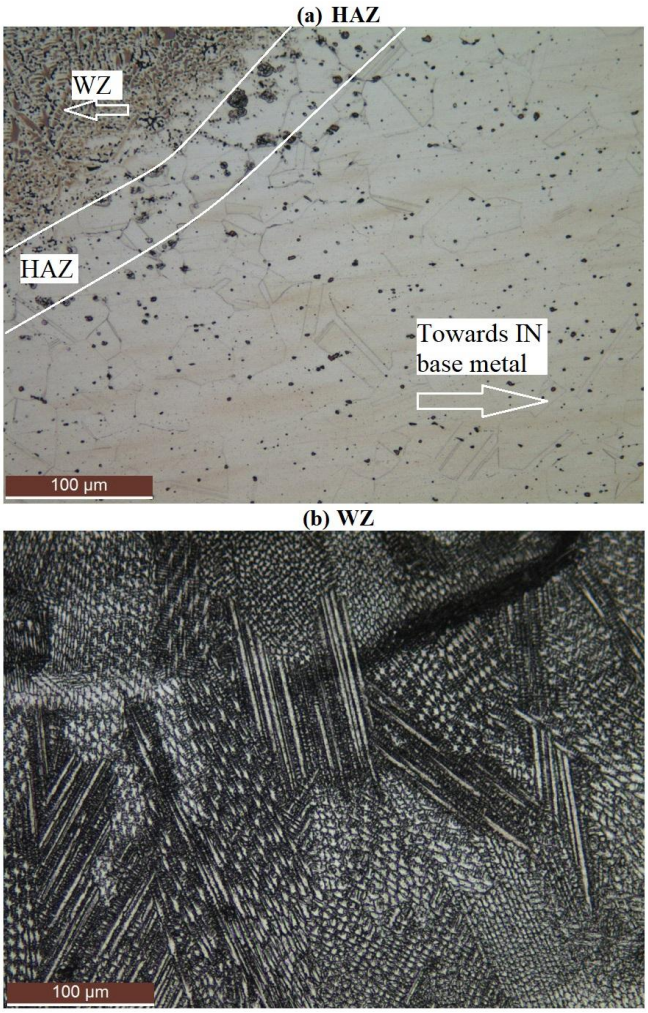

Fig. 7 Microstructural image of IN-IN welded plate with filler metal of CS: (a) Heat-affected zone; (b)Welded zone

Analysis on IN–CS welded plate using IN filler: The IN-side HAZ shows clear grain coarsening like previous IN HAZ regions. The grains adjacent to the fusion boundary are larger and slightly elongated. The deeper HAZ shows fine equiaxed grains progressing to larger grains near the fusion line (**Fig. 8a**). On the steel side, the HAZ shows partial transformation of ferrite–pearlite structure (**Fig. 8b**). Closer to the fusion line, pearlite colonies appear partially dissolved, giving rise to regions of grain-boundary ferrite and coarsened ferrite. This indicates higher peak temperatures near the fusion line, sufficient to dissolve pearlite but not enough to form martensite (expected in low-carbon steel with slow cooling). As shown in Fig. 8c, the welded zone, because the filler is IN, is Ni-rich and exhibits classical columnar dendrites. Since one base metal is CS, elemental dilution occurs, but the dendritic pattern remains predominant. The dendrites appear slightly non-uniform due to local compositional gradients created by Fe dilution from the steel side.

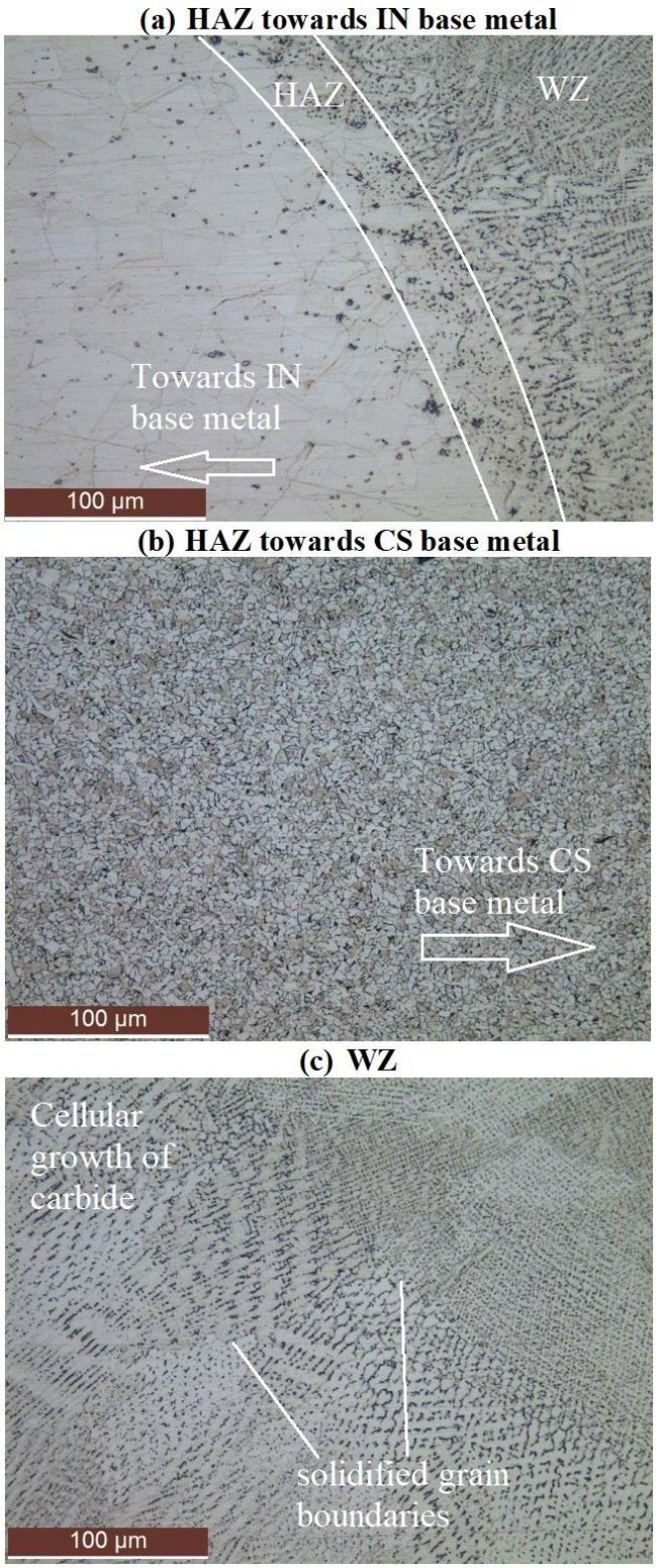

Fig. 8 Microstructural image of IN-CS welded plate with filler metal of IN: (a) Heat affected zone towards IN base metal; (b) Heat affected zone towards CS base metal; (c) Welded zone

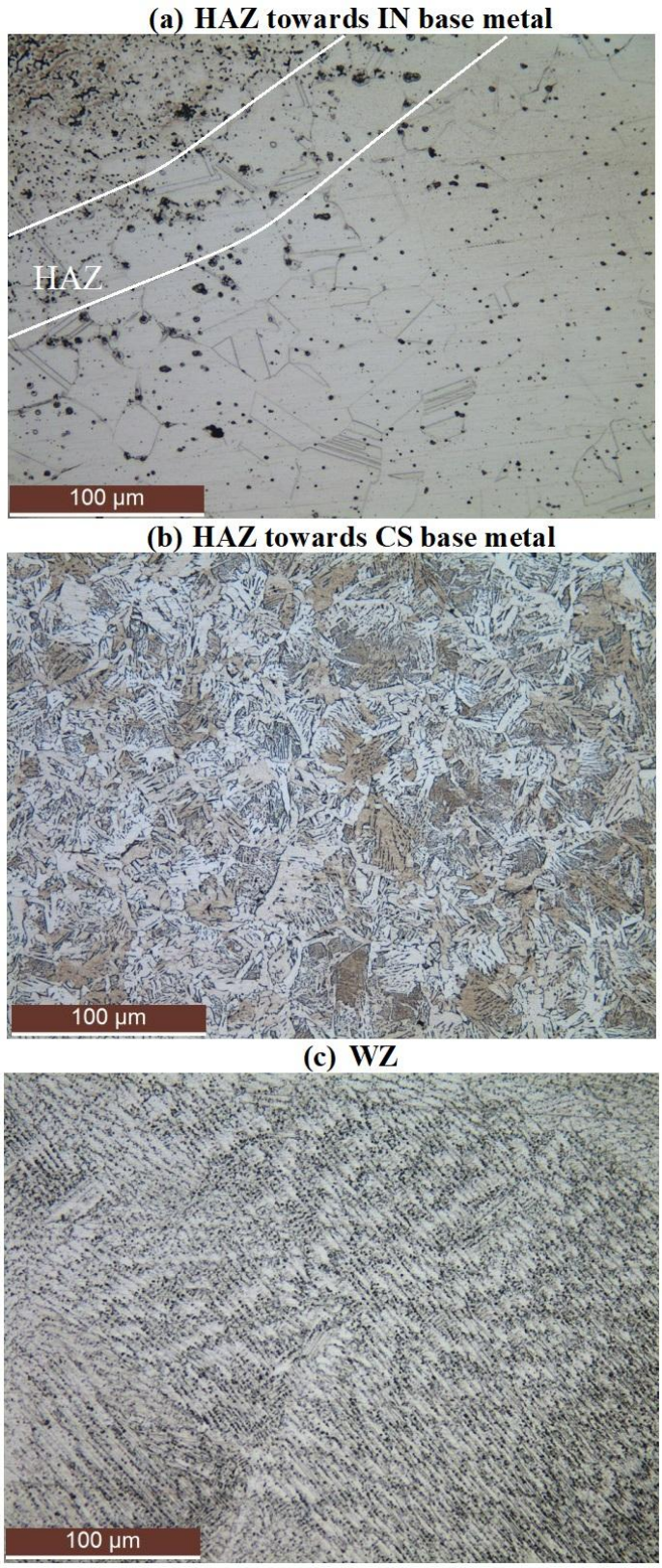

Fig. 9 Microstructural image of IN-CS welded plate with filler metal of CS: (a) Heat affected zone towards IN base metal; (b) Heat affected zone towards CS base metal; (c) Welded zone

Analysis on IN–CS welded plate using CS filler: The HAZ structure on the IN side (**Fig. 9a**) shows coarser grains compared to **Fig. 8(a)**, caused by the different thermal behavior with CS filler. Grain boundary mobility appears higher due to different heat distribution. Twins are present but less pronounced.

The CS-side HAZ in **Fig. 9b** shows significant pearlite dissolution and ferrite grain growth near the fusion boundary. This HAZ is more affected due to higher Fe dilution with the CS filler. Local etching contrast indicates ferrite grain coarsening and uneven growth characteristics typical of heat-affected low-carbon steel.

The weld zone welded with CS filler shows a fully Fe-rich dendritic matrix. The dendritic structure appears coarser and more heterogeneous than IN-filler joints due to different thermal gradients and dilution with the Ni-rich IN plate. This creates a metallurgical mismatch and visible solidification variations (**Fig. 9c**).

Analysis on CS–CS welded plate using IN filler: The HAZ shows coarsened ferrite grains and partially dissolved pearlite, similar to a high-heat weld. Because the filler is IN, the heat input and thermal distribution differ from typical CS–CS welding. The ferrite grains appear slightly elongated near the fusion line (Fig. 10a). The welded zone displays non-uniform dendritic growth. This heterogeneous structure is expected because IN filler introduces Ni-rich solidification on an otherwise Fe-rich system. This mismatch leads to a dual-phase dendritic appearance, and the etching contrast confirms differences in Ni and Fe segregation (**Fig. 10b**).

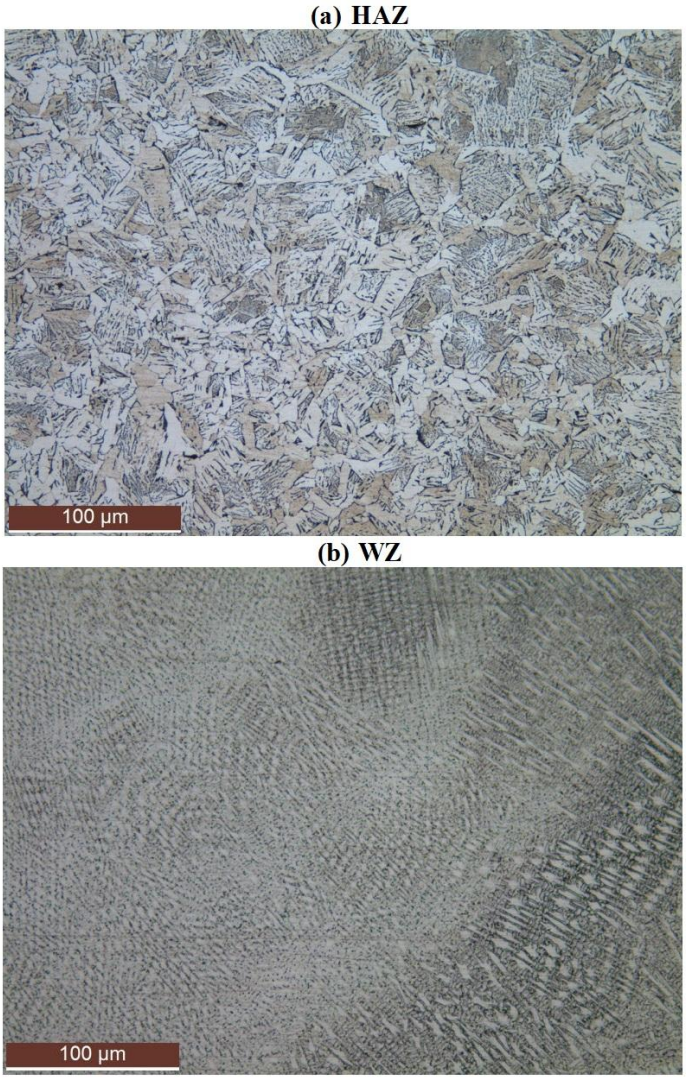

Fig. 10 Microstructural image of CS-CS welded plate with filler metal of IN: (a) Heat-affected zone; (b)Welded zone

Analysis on CS–CS welded plate using CS filler: The HAZ shows a classical low-carbon steel response: coarsened ferrite with partially dissolved pearlite near the boundary (Fig. 11a). The thermal cycle is neatly reflected in gradient grain changes from fine ferrite (far HAZ) to coarse ferrite (near fusion line). The welded zone has a typical Fe-based dendritic solidification structure, demonstrating compatibility between the CS plates and the CS filler. The dendritic structure is fine and uniform due to the absence of metallurgical mismatch. No abnormal segregation contrast is observed (**Fig. 11b**).

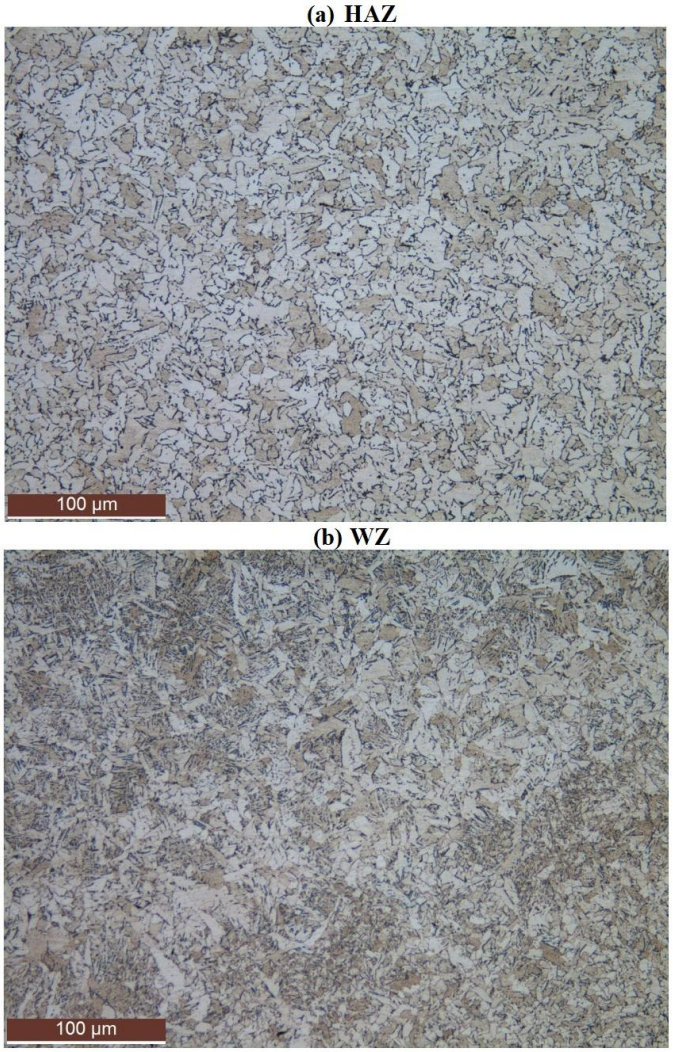

Fig. 11 Microstructural image of CS-CS welded plate with filler metal of CS: (a) Heat-affected zone; (b)Welded zone

The formation of the Nb-rich Laves phase is highly probable in both IN–IN and IN–CS welded joints due to the strong tendency of Inconel 718 to undergo interdendritic segregation of Nb, Mo, and Ti during solidification, particularly under the dendritic structures observed in the weld metal [39-42]. Even though optical microscopy cannot clearly show this intermetallic phase, it is well known that its presence reduces ductility and makes Inconel welds more brittle, which matches the weld-zone fractures seen in the tensile samples. In IN–IN welds, the higher Nb concentration and fully Ni-based composition make Laves phase formation more pronounced, thereby contributing significantly to weld-metal brittleness. In IN–CS welds made with IN filler, the mixing of iron (Fe) from the steel side reduces the amount of niobium (Nb) slightly, but small amounts of Laves phase can still form in the weld metal. This phase is hard and brittle, and even a small amount can weaken the weld by reducing its toughness. Therefore, the brittleness seen in both IN–IN and IN–CS welded joints can be partly explained by the likely formation of Laves phase in the spaces between the solidified dendrites in the weld metal.

4. CONCLUSION

This work demonstrates that the weldability and mechanical performance of Inconel 718–carbon steel combinations are strongly governed by filler metal selection, dilution behavior, and resulting microstructural transformations. This work can be concluded as follows:

- The tensile test results clearly showed that Samples 1–5 fractured in the weld zone, confirming that the fusion zone is the weakest region when Inconel is involved due to segregation, and brittle phase formation. Sample 6 (CS–CS with CS filler) demonstrated base-metal failure, proving that this weld was stronger than the parent material.
- Using matching Inconel filler for IN–IN welding (S1) produced better UTS and elongation than CS filler (S2), showing that metallurgical compatibility is essential for similar-metal joints. In dissimilar IN–CS welding, CS filler (S4) significantly improved ductility (+1134%) and strength compared to IN filler (S3), indicating that reduced mismatch and controlled dilution lead to superior performance.
- Optical micrographs revealed dendritic solidification in IN-rich welds, ferrite–pearlite transformations in CS HAZ, and heterogeneous dendritic patterns when filler–substrate mismatch was high. The likelihood of Nb-rich Laves phase and carbide formation in IN-containing welds explains the lower toughness and weld-zone fracture in most samples.
- The study confirms that welding between Inconel 718 and carbon steel is feasible, but the success of these dissimilar joints strongly depends on filler metal selection, heat input, and dilution control.

Future work should explore post-weld heat treatment (PWHT) to reduce Laves-phase-induced brittleness by promoting dissolution of segregated Nb-rich phases and lowering residual stresses in the weld metal. In the future, this study will be extended by applying PWHT to all welded configurations to evaluate its effectiveness in improving overall joint integrity.

REFERENCES

[1] CARPENTER TECHNOLOGY: (Date of access: 28-10-2025) https://www.carpentertechnology.com/alloy-finder/718

[2] Structural steel shapes: (Date of access: 05-11-2025) https://www.industrialmetalsupply.com/products/steel/structural-shapes

[3] Structural Steel Product Catalogue: (Date of access: 05-11-2025) https://www.consteel.com.sg/wpcontent/uploads/2022/09/Consteel_Catalogue_FULLspreads.pdf

[4] D. Raynor, J.M. Silcock: *Metal Science Journal*, 4(1), 1970, 121–130. https://doi.org/10.1179/msc.1970.4.1.121

[5] C.T. Sims, N.S. Stoloff, W.C. Hagel (Eds.): *Superalloys II*, Vol. 8, Wiley, New York, 1987.

[6] C. Jang, J. Lee, J.S. Kim, T.E. Jin: *International Journal of Pressure Vessels and Piping*, 85(9), 2008, 635–646. https://doi.org/10.1016/j.ijpvp.2007.08.004

[7] H. Naffakh, M. Shamanian, F. Ashrafizadeh: *Journal of Materials Processing Technology*, 209(7), 2009, 3628–3639. https://doi.org/10.1016/j.jmatprotec.2008.08.019

[8] P.P.K. Reddy, S. Dewangan, R.S. Singh, U. Singhal, A. Biswas: *Journal of The Institution of Engineers (India): Series D*, 2024, 1–12. https://doi.org/10.1007/s40033-024-00714-8

[9] S. Dewangan, S. Behera, M.K. Chowrasia: *World Journal of Engineering*, 17(1), 2020, 127–133. https://doi.org/10.1108/WJE-11-2019-0327

[10] M.D. Mathew, P. Parameswaran, K.B.S. Rao: *Materials Characterization*, 59(5), 2008, 508–513. https://doi.org/10.1016/j.matchar.2007.03.007

[11] V.G. Krishna, G.D. Janakiram, C.H.V.S. Murty, M. Srinivas, A.V. Reddy: *Practical Metallography*, 45(10), 2008, 495–504. https://link.springer.com/article/10.1007/s40032-024-01158-5

[12] W.M. Tucho, P. Cuvillier, A. Sjolyst-Kverneland, V. Hansen: *Materials Science and Engineering: A*, 689, 2017, 220–232. https://doi.org/10.1016/j.msea.2017.02.062

[13] A. Bagchi, Q. Murtaza, K. Srinivas: *Journal of Materials Engineering and Performance*, 2025. https://doi.org/10.1007/s11665-025-11848-5

[14] S. Sedighi, F. Ostovan, E. Shafiei, M. Toozandehjani: *Metallography, Microstructure, and Analysis*, 8(4), 2019, 495–505. https://doi.org/10.1007/s13632-019-00562-z

[15] D.W. Rathod, S. Pandey, S. Aravindan, P.K. Singh: *Acta Metallurgica Sinica (English Letters)*, 30(2), 2017, 120–132. https://doi.org/10.1007/s40195-016-0487-x

[16] L. Guo, F. Xiao, F. Wang *et al.*: *Journal of Failure Analysis and Prevention*, 21, 2021, 1775–1783. https://doi.org/10.1007/s11668-021-01225-4

[17] S.R. Rajesh, J. Yoo, J. Park, D. Choi: *Journal of Welding and Joining*, 40(2), 2022, 107–117. https://doi.org/10.5781/JWJ.2022.40.2.2

[18] E.P. Bossle, B. Vicharapu, G.V.B. Lemos *et al.*: *Metals*, 13(1), 2023, 146. https://doi.org/10.3390/met13010146

[19] S. Sedighi, F. Ostovan, E. Shafiei, M. Toozandehjani: *Metallography, Microstructure, and Analysis*, 8(4), 2019, 495–505. https://doi.org/10.1007/s13632-019-00562-z

[20] D. Allou, I. Ould Brahim, B. Cheniti *et al.*: *Metallography, Microstructure, and Analysis*, 10(5), 2021, 567–578. https://doi.org/10.1007/s13632-021-00773-3

[21] N. Patel: *IJSDR*, 1(5), 2016, 488–491. https://ijsdr.org/papers/IJSDR1605094.pdf

[22] P. Elango, S. Balaguru: *Indian Journal of Science and Technology*, 8(31), 2015, 1–5. https://doi.org/10.17485/ijst/2015/v8i1/84309

[23] R. Kosturek, M. Wachowski, L. Śnieżek, M. Gloc: *Metals*, 9(2), 2019, 246. https://doi.org/10.3390/met9020246

[24] S. Dewangan, S.S.S. Sunder, Y. Bhadoriya, S. Mohite, A.P. Reddy: *Journal of The Institution of Engineers (India): Series D*, 105(3), 2024, 1451–1462. https://doi.org/10.1007/s40033-023-00578-4

[25] Special Metals Corp.: *INCONEL Filler Metal 625 Datasheet*. https://www.specialmetals.com/divisions/weldingproducts/tradenames/inconel/fm625.pdf (Date of access: 05-11-2025)

[26] How to Execute the Inconel 625 Welding Procedure: https://domadia.net/how-to-execute-the-inconel-625-welding-procedure-a-step-by-step-guide/ (Date of access: 05-11-2025)

[27] Welding Technology Analysis of Inconel 625 and P22 Alloy Steel Pipes: https://www.pipeun.com/welding-technology-analysis-of-inconel-625-and-p22-alloy-steel-pipes/ (Date of access: 05-11-2025)

[28] G.D. Janaki Ram, A. Venugopal Reddy, K. Prasad Rao, G. Madhusudhan Reddy: *Science and Technology of Welding and Joining*, 9(5), 2004, 390–398. https://doi.org/10.1179/136217104225021788

[29] A. Sahadevan, R.K. Ilangovan, N.T.B.N. Koundinya *et al.*: *Journal of Materials Engineering and Performance*, 2025, 1–15. https://doi.org/10.1007/s11665-025-12331-x

[30] J.J. Schirra, R.H. Caless, R.W. Hatala: *Superalloys 718, 625 and Various Derivatives*, TMS, 1991, 375–388. https://www.tms.org/superalloys/10.7449/1991/Superalloys_1991_375_388.pdf

[31] E. Bassini, G. Marchese, A. Aversa: *Metals*, 11(6), 2021, 921. https://doi.org/10.3390/met11060921

[32] G.M.D. Almaraz, M.G. Tapia, I.F.Z. Tello: *Procedia Structural Integrity*, 39, 2022, 281–289. https://doi.org/10.1016/j.prostr.2022.03.098

[33] P. Bai, P. Huo, J. Wang *et al.*: *Journal of Alloys and Compounds*, 911, 2022, 164988. https://doi.org/10.1016/j.jallcom.2022.164988

[34] T. Sonar, V. Balasubramanian, S. Malarvizhi *et al.*: *Materials Characterization*, 174, 2021, 110997. https://doi.org/10.1016/j.matchar.2021.110997

[35] S.A. Kumar *et al.*: *Materials Science and Engineering: A*, 807, 2021, 140894. https://doi.org/10.1016/j.matchar.2021.110997

[36] K. Motham, S. Khamsuk, H. Miura, A.S. Anasyida: *Journal of Physics: Conference Series*, 1082(1), 2018, 012067. https://doi.org/10.1088/1742-6596/1082/1/012067

[37] S. Dewangan, V.V. Nemade, K.H. Nemade: *Acta Metallurgica Slovaca*, 29(1), 2023, 26–33. https://doi.org/10.36547/ams.29.1.1719

[38] N. Yamaguchi, G. Lemoine, T. Shiozaki, Y. Tamai: *International Journal of Fatigue*, 129, 2019, 105233. https://doi.org/10.1016/j.ijfatigue.2019.105233

[39] M.B. Henderson, D. Arrell, R. Larsson, M. Heobel, G. Marchant: *Science and Technology of Welding and Joining*, 9, 2004, 13–21. https://doi.org/10.1179/136217104225017099

[40] G. Ressel, F. Biermair, S. Fellner *et al.*: *Scientific Reports*, 13(1), 2023, 16874. https://www.nature.com/articles/s41598-023-43722-6.pdf

[41] T. Sonar, V. Balasubramanian, S. Malarvizhi *et al.*: *Australian Journal of Mechanical Engineering*, 2020. https://doi.org/10.1080/14484846.2020.1794512

[42] H.J. Wagner, A. Hall: *Physical Metallurgy of Alloy 718*, DMIC Report 217, Battelle Memorial Institute, Columbus, Ohio, 1965.